Sumit R. Zanje¹

Department of Civil and Environmental Engineering, Florida International University, Miami, FL 33174 e-mail: szanj001@fiu.edu

Linlong Bian

Department of Civil and Environmental Engineering, Florida International University, Miami, FL 33174 e-mail: Ibian003@fiu.edu

Vivek Verma

Department of Civil and Environmental Engineering, Florida International University, Miami, FL 33174 e-mail: vverm002@fiu.edu

Zeda Yin

Department of Civil and Environmental Engineering, Florida International University, Miami, FL 33174 e-mail: zyin005@fiu.edu

Arturo S. Leon

Department of Civil and Environmental Engineering, Florida International University, Miami, FL 33174 e-mail: arleon@fiu.edu

Siphon Break Phenomena Associated With Pipe Leakage Location

This work investigates the siphon break phenomenon associated with pipe leakage location. The present study is divided into two parts: (1) an unsteady three-dimensional (3D) computational fluid dynamics (CFD) model is developed to simulate the pressure head (water level) and discharge in the simulated siphon using the volume-of-fluid (VOF) technique under no-leakage condition and (2) using the model developed in the first part we investigated the siphon break phenomenon associated with pipe leakage location. The calculated results of transient water level and discharge rate at the simulated siphon for the no-leakage condition were in good agreement with the experimental measurements. In addition, the velocity, pressure fields, and phase fractions in the siphon pipe were analyzed in depth. The methodology and findings presented show that leakage above the hydraulic grade line and close to the top inverted U section of the siphon pipe ultimately leads to the siphon breakage, which is not the case for a leakage below the hydraulic grade line. It is also concluded that if leakage is above the hydraulic grade line and the leakage position is far away from the upper horizontal section of the siphon pipe, it may not lead to the immediate siphon breakage as ingested air gets removed with siphoning water, allowing it further time to cause complete siphon breakage.

[DOI: 10.1115/1.4054654]

Introduction

A siphon essentially consists of an inverted "U" pipe, one end of which is held in contact with the reservoir on the upstream side, and the other end discharges liquid at the downstream end, as indicated in Fig. 1 [1,2]. Siphons have been known since ancient times as simple and low-cost devices for transferring water using gravitational force. The siphon operates due to a pressure difference between the ambient pressure at the upper reservoir and the top of the siphon (negative gauge pressure). A Siphon system is usually selected compared to the pump system in operation and safety of dams where space is limited, and the discharge is not excessively high. The siphon will drain liquid from the upstream reservoir until the liquid level falls below the inlet of the invert pipe, allowing air to break the siphon flow or until the siphon outlet equals the level of liquid in the upstream reservoir, whichever occurs first. To prevent air entry into the system, the downstream end of the siphon may be submerged [3]. A critical aspect of siphon design is the minimum water surface elevation in the upstream reservoir relative to the top of the siphon. The siphon will not work if the elevation difference is too high. When this elevation difference is very high, liquid pressure drops below the vapor pressure, causing the formation of tiny vapor bubbles. This may interrupt the flow and may even cause pipe collapse. One of the advantages of a siphon system is that the maintenance with an actively running siphon can be lower than a pumping system. Finally, once a properly mounted siphon is operational, no power source is needed. Nonetheless, traditional architecture could only be effective in limited diameter and low lift head applications. An efficient and novel air management system is needed for large diameter and high lift heads.

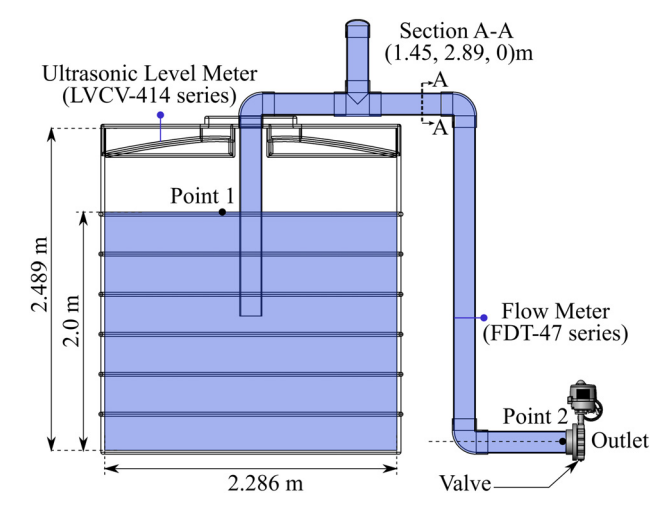


Fig. 1 Schematic diagram of experimental siphon facility

¹Corresponding author.

Contributed by the Fluids Engineering Division of ASME for publication in the JOURNAL OF FLUIDS ENGINEERING. Manuscript received August 30, 2021; final manuscript received May 17, 2022; published online June 15, 2022. Assoc. Editor: S. A. Sherif.

Many researchers reviewed this phenomenon to understand the mechanism of its working [4–7]. Ervine [8] and Ervine and Oliver [9] characterized the air-regulated siphon in four stages and concluded that it's possible to achieve a desired stable discharge with a well-designed air slot. Babaeyan-Koopaei et al. [10] provided a detailed explanation of siphon spillways operating stages. Hughes [5] is notable for discovering a 99-year-old error in the Oxford dictionary and correcting the operating force of a siphon, which is gravity rather than atmospheric pressure. Viridi et al. [11] demonstrated the maximum value of siphon height, where the selfsiphon still can flow the water using the molecular dynamics (MD) method. Cai et al. [12] experimentally investigated flow pattern variables and relevant influencing factors at the top of siphon hoses on drainage flow. Leon and Alnahit [13] demonstrated drainage of a tank by siphonage. Although the study lacked detailed flow field visualization using numerical simulations, the authors found a good agreement when comparing results using the energy equation, measured experimental data, and threedimensional (3D) numerical simulations. Aydin et al. [14] investigated the hydrodynamic characteristics of siphon using volume-of-fluid formulation. The study showed that an error between the experiments and computational fluid dynamics (CFD) results with respect to the discharge performance was obtained as 11% of the relative mean error, probably because of fluctuations due to air entrainment into the siphon and the measurement errors.

Additionally, a number of studies have focused on understanding the siphon breakage phenomenon. Kang et al. [15] experimentally investigated the effect of the size and type of the siphon breaker, the size and position of a loss-of-coolant accident, and the presence of an orifice on siphon performance. Park et al. [16] used 3D two-phase transient flow analysis code to assess the siphonage flow rate and siphon break phenomena. Ramajo et al. [17] numerically investigated the siphon breaker system using two siphon breaker lines (SBL) and one siphon breaker hole (SBH). All of the above siphon-breaking research is based on particular applications or individual needs. It is hard to extend to other systems as system size significantly impacts the siphon-break phenomenon.

This study is part of our flood control project using dynamic management of landscape water storage, which is made possible through remotely operated siphons. For the success of the overall process, it is important to maintain the siphon primed (i.e., full of water) and thus free of leaks. In our preliminary siphon implementations, the siphon would require periodic priming due to leaks. This study aims to investigate the hydrodynamic characteristics of a siphon and analyze the siphon break phenomenon caused by leaks in the siphon pipe and when the water level falls below the inlet elevation. A detailed understanding of two-phase dynamics using 3D numerical simulations will help understand the role of the size and location of leaks in maintaining the siphon flow. This paper is divided as follows: First, experimental work is presented for the no-leakage condition. Second, a CFD model is developed using OpenFOAM [18] and validated using the experimental data. Third, the validated CFD model is used to investigate the siphon break phenomenon associated with a leakage in the siphon pipe and when the liquid falls below the inlet invert pipe. Fourth, the results for no-leakage and leakage conditions are presented and discussed. Finally, the key remarks are made in the conclusion section.

Experimental Work

The experimental facility was conducted at the Engineering Center (EC) of the Florida International University (FIU), Miami, FL

Measurement Equipment. The measurement equipment used in the study includes:

 One ultrasonic level sensor and controller (LVCN-414 Series) (range of 1.25 m, accuracy of 3 mm, and resolution of 0.5 mm).

- (2) One flow meter (FDT-47 Series with V mounting style) (velocity range of 0.01 to 40 FPS, accuracy of $\pm 1\%$, and repeatability of 0.5% of reading).
- (3) One National Instruments data acquisition board NI 6323 with SCB 68A Terminal and sampling rate up to 250 kHz integrated with LabVIEW.

Experimental Setup. The apparatus for the experimental study is shown schematically in Fig. 1. The siphon consisted of PVC pipe schedule 40 with an internal diameter (D) of 0.152 m (6 in) and an actuated butterfly valve at the outlet. The total length of the siphon pipe is approximately 7.6 m (25 ft). The water tank has a maximum capacity of 2,500 gals with a diameter of 90 inches and a height of 98 inches. A check valve is used at the pipe inlet to prevent backward flow. A bilge pump is used for the siphon priming. An extended sight tube consisted of clear PVC schedule 40 with an internal diameter of 0.152 m (6 in) provided to visualize and control the priming. An air vent and two-level switches are connected to the sight tube to control the priming, as shown in Fig. 2. The water level in the tank was measured using the LVCN-414 level meter sensor and discharge in the pipe by FDT-47 with V mounting style connected to NI 6323 X Series data acquisition with SCB 68 A terminal. The data collected in the experiments include discharge rate (Q) and the water elevation in the tank (H).

Analytical Model

Siphon flow is analyzed using the energy equation, as shown in Eq. (1)

$$Z_1 + \frac{P_1}{\gamma} + \frac{v_1^2}{2g} = Z_2 + \frac{P_2}{\gamma} + \frac{v_2^2}{2g} + h_f + h_l \tag{1}$$

where, Z_1 is the elevation of water surface in the tank (Point 1), Z_2 is the elevation of the pipe centerline at the outlet (Point 2), P_1 and P_2 are pressure at points 1 and 2, respectively, v_1 and v_2 are cross-sectional averaged velocities at points 1 and 2, respectively, γ is the specific weight of the water, g is the acceleration due to gravity, h_f is total head loss due to pipe friction, h_l is the sum of local head losses. The total head loss due to friction using the Darcy-Weisbach formula is given by Eq. (2) [19–21]

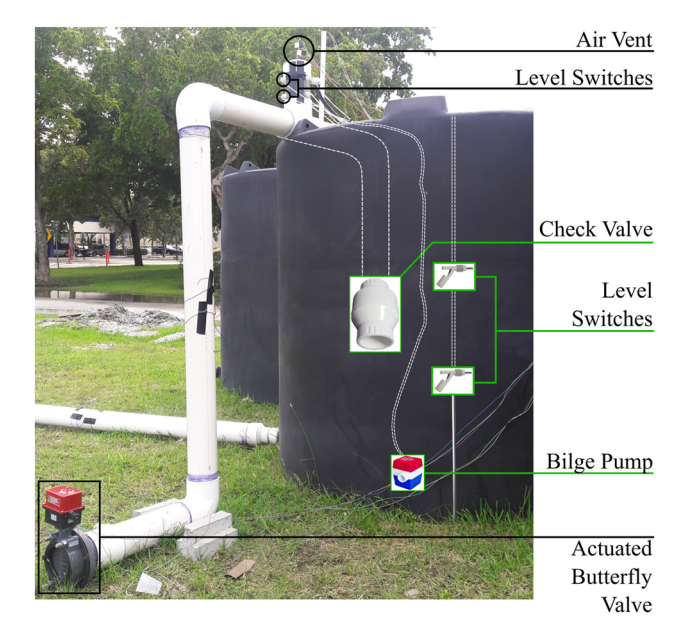


Fig. 2 Photograph of the siphon experimental facility with primary components

$$h_f = \frac{fLv^2}{2gD} \tag{2}$$

where, f is the friction factor, L is the total length of the siphon pipe, v is pipe cross-sectional averaged flow velocity, and D is the siphon pipe diameter. The local head loss (h_l) is given by Eq. (3) [22–24]

$$h_l = \sum k \frac{v^2}{2g} \tag{3}$$

where, *k* is the head loss coefficient for the pipe fittings (i.e., check valve, butterfly valve, elbows, etc..). In addition to Eq. (1), flow should also meet the continuity equation, as shown in Eq. (4)

$$Av_1 = A_d v_2 \tag{4}$$

where, A is the area of the base of the storage tank and A_d is the cross-sectional area of the siphon pipe. From Eqs. (1) to (4), the velocity (v) and discharge rate (Q) as a function of water level (H) can be derived as Eqs. (5) and (6) below

$$v = \left(\frac{2gH}{1 + \sum k + f\frac{L}{D}}\right)^{\frac{1}{2}} \tag{5}$$

$$Q = \frac{\pi}{4}D^2 \times \left(\frac{2gH}{1 + \sum k + f\frac{L}{D}}\right)^{\frac{1}{2}} \tag{6}$$

Within an infinitesimal time interval (dt), the water volume decreased in the tank and the water volume flow outside of the tank should meet the relationship as shown in Eq. (7)

$$dV = Q(h)dt = \frac{\pi}{4}D^2 \times \left(\frac{2g}{1 + \sum k + f\frac{L}{D}}\right)^{\frac{1}{2}} \times \sqrt{h}dt$$
 (7)

where, dV also can be expressed as the Eq. (8) below

$$-dV = A \times dh \tag{8}$$

where, dV is the water volume decreased in the tank and dh is the water level decreased in the tank. Using Eqs. (7) and (8), the relationship between time (t) and water depth is as shown in Eq. (9) below

$$\int_{0}^{t} dt = -\chi \int_{H_{a}}^{H} \frac{1}{\sqrt{h}} dh \tag{9}$$

where, H_0 is the initial water depth and χ is a constant parameter which is expressed below

$$\chi = \frac{A}{\frac{\pi D^2}{4} \left(\frac{2g}{1 + \sum k + f \frac{L}{D}} \right)^{\frac{1}{2}}}$$
 (10)

The friction factor f can be obtained using the Haaland equation [25], as shown below

$$\frac{1}{\sqrt{f}} = -1.8 \log_{10} \left[\frac{6.9}{Re} + \left(\frac{\varepsilon}{3.7D} \right)^{1.1} \right]$$
 (11)

where, ε is roughness height and Re is Reynolds number. The unsteady water elevation (H) in the storage tank is calculated using Eq. (9)

$$H = \frac{1}{4\chi^2}t^2 - \frac{\sqrt{H_0}}{\chi}t + H_0 \tag{12}$$

Using Eqs. (5) and (9), the relationship between time (t) and velocity (v) is calculated as shown in Eq. (13) below

$$t = 2\chi \left(\sqrt{H_0} - \frac{1}{\sqrt{\frac{2g}{1 + \sum k + f\frac{L}{D}}}} v \right)$$
 (13)

Therefore, using Eq. (13), siphon flow rate (Q) is calculated analytically using Eq. (14)

$$Q = -\frac{\pi D^{2} A_{d}}{4A} \left(\frac{2g}{1 + \sum k} \right) t + A_{d} \sqrt{\frac{2g}{1 + \sum k + f \frac{L}{D}}} \sqrt{H_{0}}$$
 (14)

Numerical Model

Governing Equations. In this study OpenFOAM 6.0 is used to numerically simulate the fluid flow [26]. The OpenFOAM solver has previously been tested for multiphase flow simulation [17,27]. Considering the physics of siphon and previous numerical studies [17], an interFoam solver was chosen in this study [28]. This solver uses the volume of fluid to capture the fluid interface (herein, water and air). The volume of fluid uses a scalar function (α) , called the liquid phase fraction, to define the water region $(\alpha=1)$ and air region $(\alpha=0)$ [29]. The Reynolds-averaged Navier–Stokes equations for unsteady incompressible flow are shown below

$$\nabla \cdot \boldsymbol{u} = 0 \tag{15}$$

$$\frac{\partial(\rho \mathbf{u})}{\partial t} + \nabla \cdot (\rho \mathbf{u} \mathbf{u}) = -\nabla p_d + \nabla \cdot \mathbf{T} - \mathbf{g} \cdot \mathbf{x} \nabla \rho + \sigma \kappa \nabla \alpha \quad (16)$$

where, u is the velocity vector, T is a deviatoric stress tensor, x is the position vector, g (0, -9.81, 0) is the gravitational vector, σ is the surface tension coefficient, and the local curvature of the free surface is calculated as $\kappa = -\nabla \cdot (\nabla \alpha/|\alpha|)$. The $\nabla \cdot T$ term in Eq. (16) can also be represented as follows:

$$\nabla \cdot \mathbf{T} = \nabla \cdot (\mu \nabla \mathbf{u}) + \nabla \mathbf{u} \cdot \nabla \mu \tag{17}$$

In addition to Eqs. (15) and (16), for tracking the air—water interface, a transport equation for the phase fraction is solved as shown in Eq. (18)

$$\frac{\partial \alpha}{\partial t} + \nabla \cdot (\boldsymbol{u}\alpha) + \nabla \cdot [\boldsymbol{u}_{\mathbf{r}}\alpha(1-\alpha)] = 0$$
 (18)

where, u_r is liquid–gas relative velocity. The relative flux appearing in the Eq. (18) is replaced with the compression flux acting normal to the interface and functioning only within the thin interface region. Further details about this method and its implementation are given in Berberović et al. [30] and Berberović et al. [31]. The fluid properties such as dynamic viscosity (μ) and density (ρ) in each computational cell can be obtained as follows:

$$\mu = \alpha \mu_w + (1 - \alpha)\mu_a \tag{19}$$

$$\rho = \alpha \rho_w + (1 - \alpha)\rho_a \tag{20}$$

The indexes w and a represents water and air, respectively. The term p_d in Eq. (16) is modified pressure, avoiding dependency of p on elevation, and makes the specification of boundary condition simpler [32]

$$p_d = p - \rho \mathbf{g} \cdot \mathbf{x} \tag{21}$$

The momentum Eq. (22) is dependent on the volume fractions of air and water through the ρ and μ

$$\frac{\partial(\rho \mathbf{u})}{\partial t} + \nabla \cdot (\rho \mathbf{u} \mathbf{u}) - \nabla(\mu \nabla \mathbf{u}) - \nabla \mathbf{u} \cdot \nabla \mu$$

$$= -\nabla p_d - \mathbf{g} \cdot \mathbf{x} \nabla \rho + \sigma \kappa \nabla \alpha \tag{22}$$

Regarding turbulence modeling, Ramajo et al. [17] showed that standard $\kappa - \varepsilon$ is suitable for capturing the siphonage phenomena. Therefore, this model with the log-law wall function is used for all the simulations performed in the current study [33]. It is noted that the standard $\kappa - \varepsilon$ model is implemented in OpenFOAM based on Launder and Spalding [34]. It is worth mentioning that the Bond number $(B_o = (\rho_w - \rho_a)gD^2/\sigma)$ value in our case is 3228, which indicates that the system is unaffected by the effect of surface tension (σ) [35]. The validity of this statement was tested with two simulations for the no-puncture case; one with a surface tension value of 0.072 N/m and another with zero. The results showed identical water elevation and discharge rate time traces that surface tension has negligible influence as expected. In addition, the Capillary number (Ca = $\mu V/\sigma$) ranges from 0.0197 to 0.0346, indicating that the capillary forces are insignificant compared to the viscous forces [36].

Computational Domain and Geometry. This study involves four different computational domains: one without leakage (Fig. 3(a)) validated using experimental results, two with leakage (Figs. 3(b)) and 3(c)) above the hydraulic grade line, and the last case (Fig. 3(d)) with the initial position of leakage below the hydraulic grade line. Figure 3 shows a computational geometry with the main dimensions of the siphon system. The water tank is a cylinder of 90 inches in diameter and 98 inches in height with a total volume of 2500 gals. The siphon pipe diameter is $0.152 \,\mathrm{m}$ (6 in). The siphon pipe has three 90 deg elbows. To represent the flow obstruction due to the butterfly valve at the pipe outlet cross section area was reduced by 58%. This value was obtained using manual specifications (dimensions) for the selected butterfly valve series and after performing numerical iterations to match the slope of discharge time trace with experimental data. In addition, an

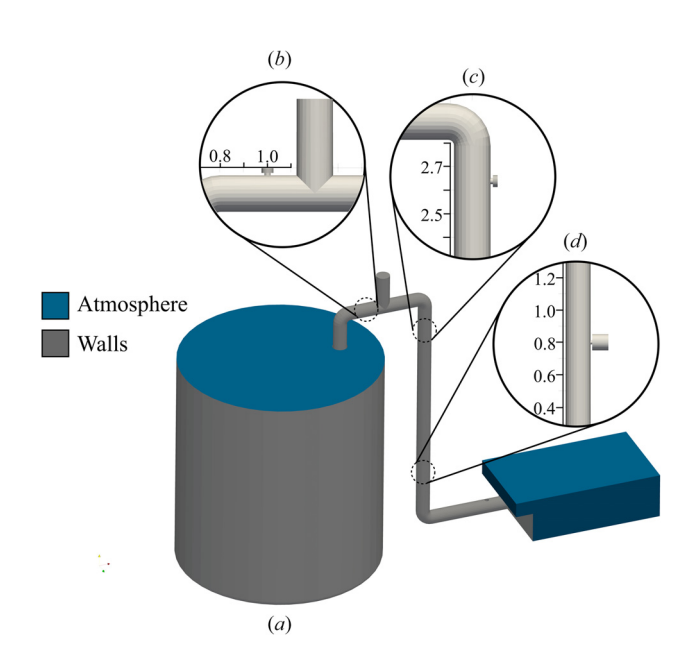


Fig. 3 View of the computational geometries with the main parameters: (a) no-leakage, (b) leakage case-1, (c) leakage case-2, and (d) leakage case-3

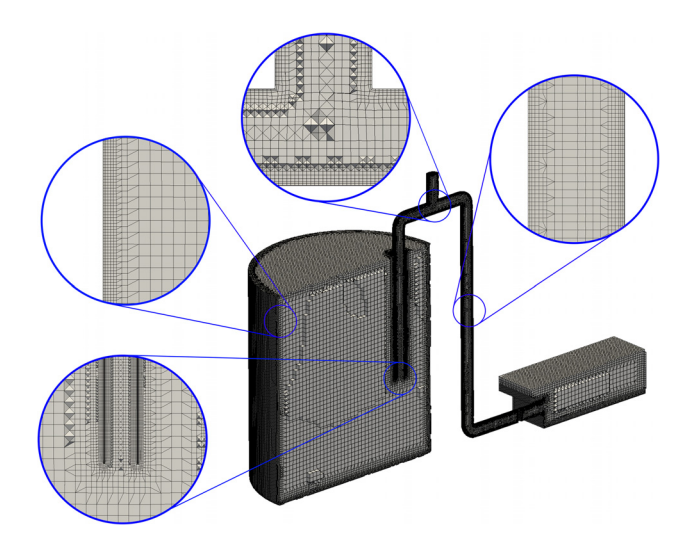


Fig. 4 View of 3D mesh used for computational setup (no-leakage)

extended computational domain was provided at the pipe outlet to avoid imposing an atmospheric pressure boundary condition at the pipe outlet, which leads to artificial instabilities in the siphon. The total height from the storage tank's base to the bottom of the siphon pipe inside the tank is 1 m. Due to high computational cost, in this paper, only a case with an initial water elevation of 2 m was used to validate the computational model.

Figure 4 shows a detailed 3D mesh generated using *snappyHex*-Mesh, an OpenFOAM meshing utility. The hybrid mesh was selected due to its suitability to match appropriate cells with the boundary surface and allocate different cells of various element types in other parts of the complex flow regions. It leads to an accurate solution and better convergence than using only either structured or unstructured mesh [37]. As shown in Fig. 4, the siphon pipe was refined compared to the tank. The mesh size transition was achieved carefully between pipe and water tank mesh. A mesh convergence study was carried out to determine the most efficient mesh size in terms of accuracy and computation time. Starting from a coarse mesh (with the overall mesh had 1,121,410 cells), the mesh was refined by a factor of two to generate a new mesh. After each refinement, the obtained numerical results were compared with the experimental data. This process was repeated until the results of the refined mesh were in close agreement with the previous mesh and the experimental data.

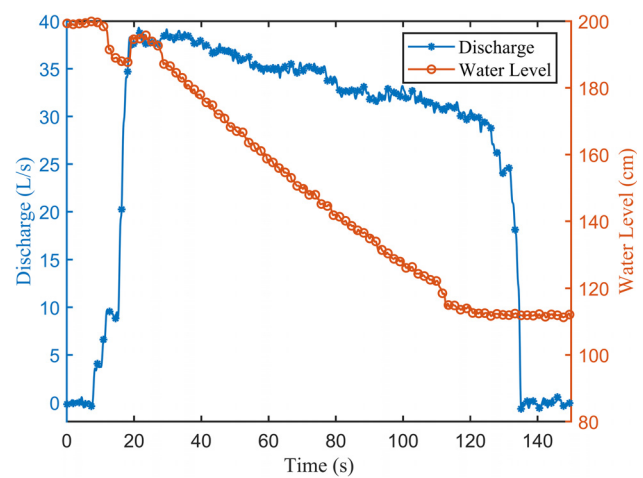


Fig. 5 Measured water level and flow discharge data measured for no-leakage case

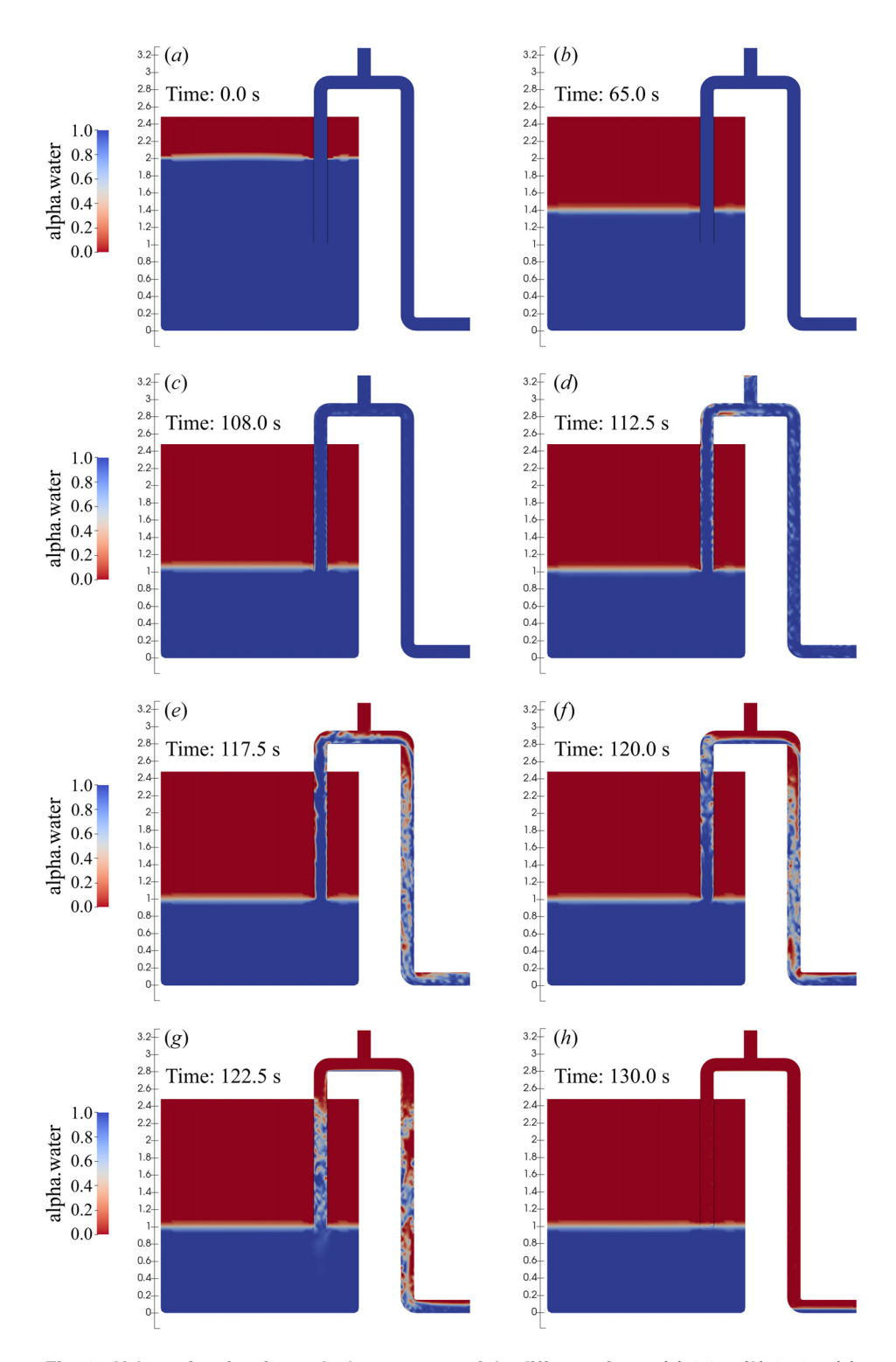


Fig. 6 Volume fraction for no-leakage case at eight different times: (a) $0.0 \, \text{s}$, (b) $65.0 \, \text{s}$, (c) $108.0 \, \text{s}$, (d) $112.5 \, \text{s}$, (e) $117.5 \, \text{s}$, (f) $120.0 \, \text{s}$, (g) $122.5 \, \text{s}$, and (h) $130.0 \, \text{s}$

Boundary and Initial Conditions. The top surface of the water tank and the extended domain is open to the atmosphere with a total pressure value set to $101,600 \, \text{N/m}^2$ (pressure recorded during experimentation). For the tank and pipe, the wall no-slip boundary condition was used for velocity (i.e., fixedValue u=0) and zerogradient for other fields. Considering the standard $\kappa-\varepsilon$ turbulence model, the walls were modeled using wall functions for turbulence kinetic energy (κ) and turbulence dissipation rate (ε) . The tank was initially filled to the 2 m elevation, and the siphon was

primed (i.e., the pipe is filled with zero water velocity) using *set-Fields* utility.

Numerical Settings. The simulation was run on 32 processors using the distributed parallel *decomposePar* computing utility (AMD Ryzen Threadripper 3960X 3.8 GHz 32-Core sTRX4 Processor). Adjustable time steps with the maximum Courant number $(C = u\Delta t/\Delta x)$ was set to 0.75. Additionally, in this study, a first-

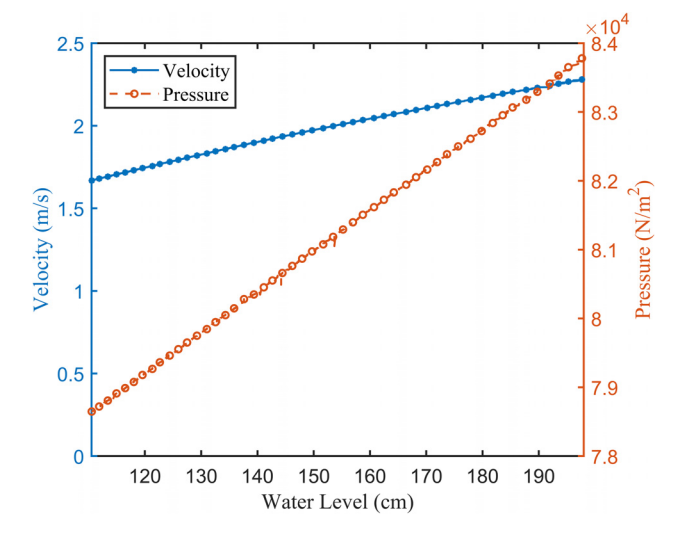


Fig. 7 Water velocity and pressure at section A-A (Operator: weightedAreaIntegrate; weightField: alpha.water) in Fig. 1 according to the tank water level (no-leakage)

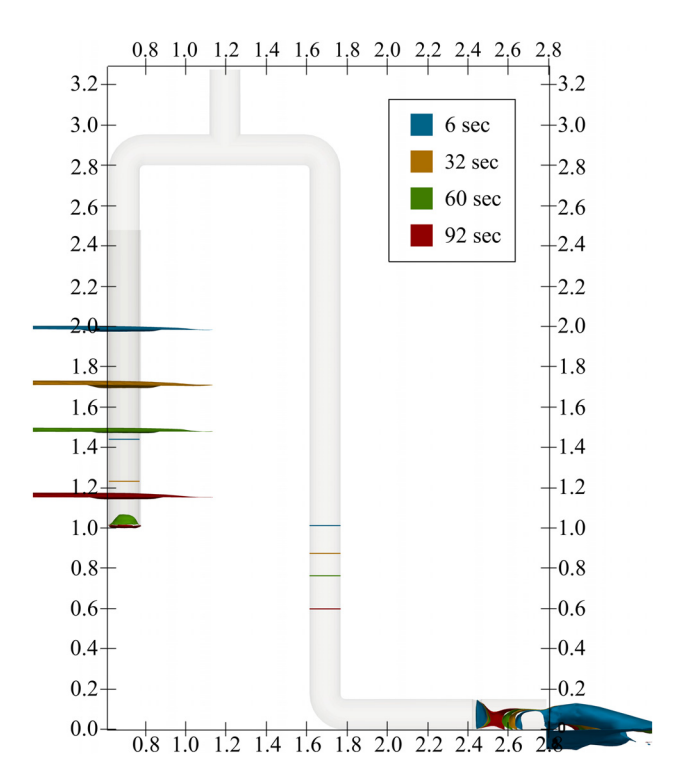


Fig. 8 Isobaric surface plots for atmospheric pressure $(101,600\,\text{N/m}^2)$ for siphon under the no-leakage condition

order implicit temporal scheme is used, and a second-order scheme was considered for spatial distribution [38].

Results and Discussion

Experimental Results. This experimental study examined the variation of water level (H) in the tank and discharge rate (Q) in the siphon with time. Figure 5 shows the complete time trace for the water elevation (a solid line with circle markers) in the tank and the discharge (a solid line with asterisk markers) in the siphon. The jump around the 5th second implies the siphon has started its operation, i.e., the butterfly valve opens, and the water starts flowing out of the tank. Similarly, a sudden drop at around 145th second indicates that the butterfly valve is completely

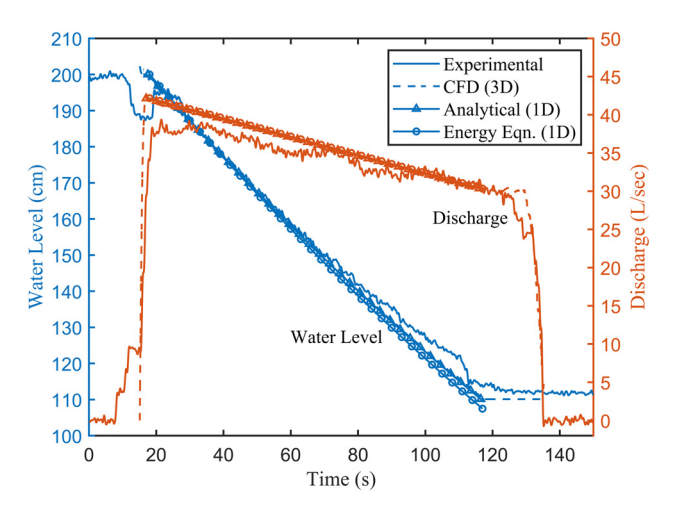


Fig. 9 Comparison of experimental, numerical, analytical, and energy equation results for water level and discharge rate. [Note: The numerical sampling of discharge rate is done using 'weightedVolAverage' operator with 'alpha.water' as a weighting field, whereas the water level variation is sampled in Para-View using 'IntegrateVariables' operator]

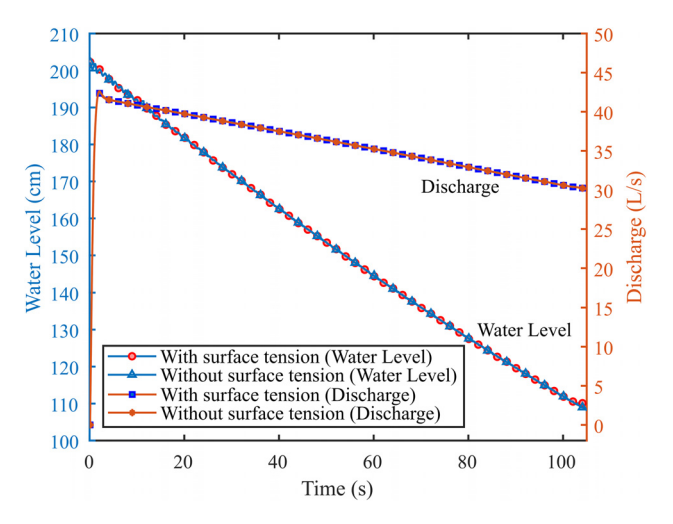


Fig. 10 Result of simulations with surface tension and without surface tension for water level and discharge rate

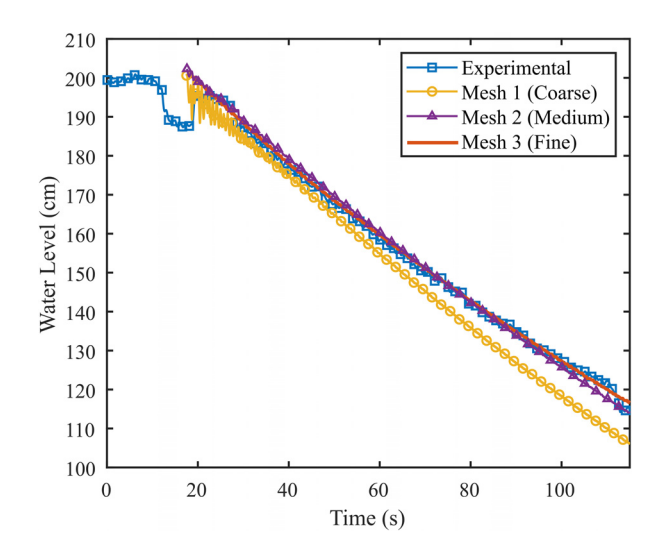


Fig. 11 Results of simulations for the mesh convergence study for water level

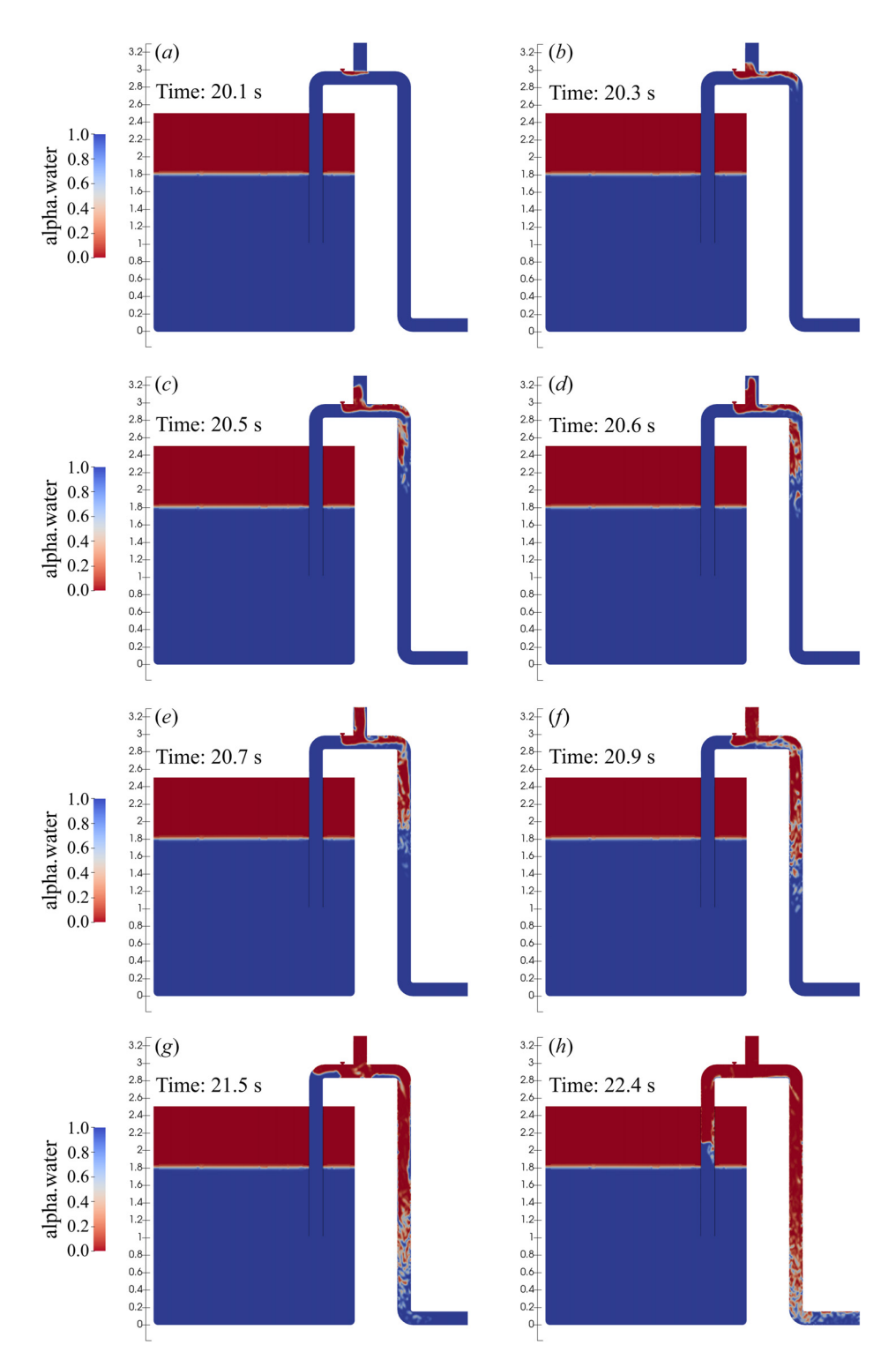


Fig. 12 Water volume fraction for leakage case-1 at eight different times: (a) $20.1 \, \text{s}$, (b) $20.3 \, \text{s}$, (c) $20.5 \, \text{s}$, (d) $20.6 \, \text{s}$, (e) $20.7 \, \text{s}$, (f) $20.9 \, \text{s}$, (g) $21.5 \, \text{s}$, and (h) $22.4 \, \text{s}$

closed, so discharge becomes zero. The maximum flow recorded by the instrument FDT-47 is about 40 L/s at around 25th second, related to a water depth of 1.94 m. Further details on experimental data acquisition and uncertainty analysis are presented in previous studies conducted by Ref. [39].

Numerical Results. The four numerically simulated cases are (Fig. 3):

(1) Siphon without leakage (no-leakage case): A numerical model based on the experimental setup. The numerical

- results are validated with the experimental data (H versus Time (t) and Q versus Time (t)).
- (2) Siphon with leakage (case-1): A hole of diameter (d_l) 1 inch is provided at the top portion of the siphon pipe after 20 s of siphon flow. The position of the leakage is above the hydraulic grade line.
- (3) Siphon with leakage (case-2): A hole of diameter (d_i) 1 inch is provided at the upper side of the downgoing limb of the pipe after 20 s of siphon flow. The position of the leakage is above the hydraulic grade line.

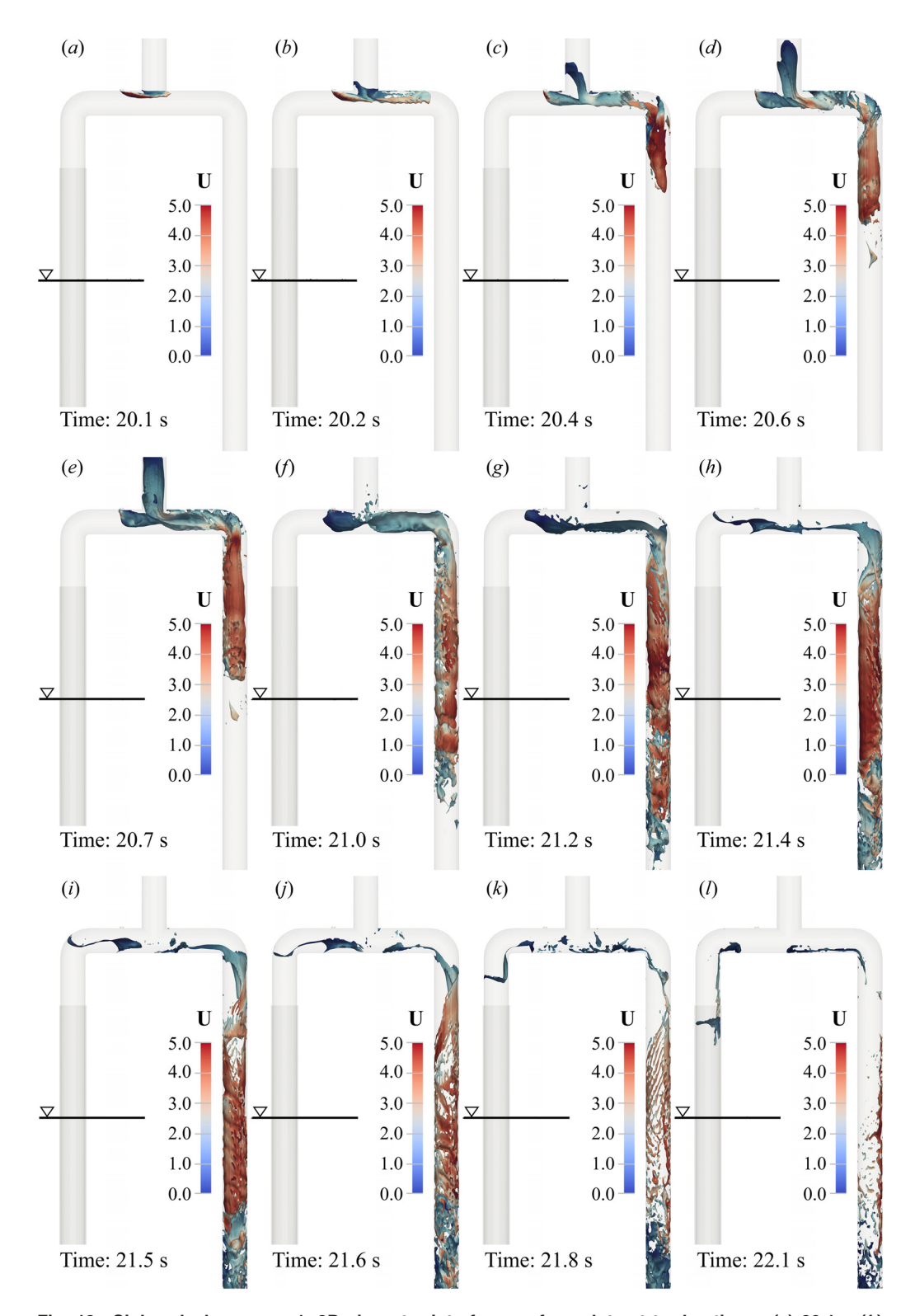


Fig. 13 Siphon leakage case-1. 3D air—water interface surface plots at twelve times: (a) $20.1 \, s$, (b) $20.2 \, s$, (c) $20.4 \, s$, (d) $20.6 \, s$, (e) $20.7 \, s$, (f) $21.0 \, s$, (g) $21.2 \, s$, (h) $21.4 \, s$, (i) $21.5 \, s$, (j) $21.6 \, s$, (k) $21.8 \, s$, and (l) $22.1 \, s$

(4) Siphon with leakage (case-3): A hole of diameter (d_i) 1 inch is provided at the lower side of the downgoing limb of the pipe. The initial position of the leakage is below the hydraulic grade line.

Siphon Without Leakage (No-Leakage) Condition. Figure 6 shows the simulated air-water phase fraction data at the center

plane for the no-leakage condition at eight different times. At t=0 s, the level of water in the storage tank is 2 m, and the siphon pipe is completely filled with water. This state corresponds to that after priming. At t=65 s, the water level reduces to 1.4 m. At t=108 seconds, the air started entering the inlet pipe. From this time onward, phases are largely segregated as more and more air starts entering the system. At t=120 s, the air fraction in the system is very large, stopping the siphoning effect.

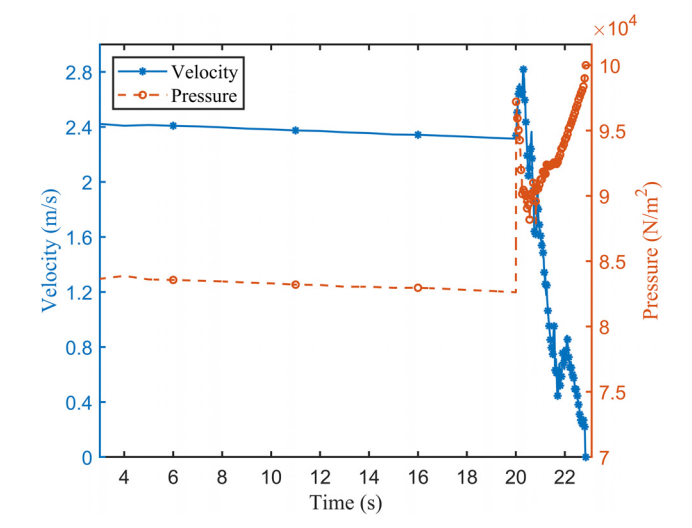


Fig. 14 Water velocity and pressure time trace at section A-A for leakage case-1

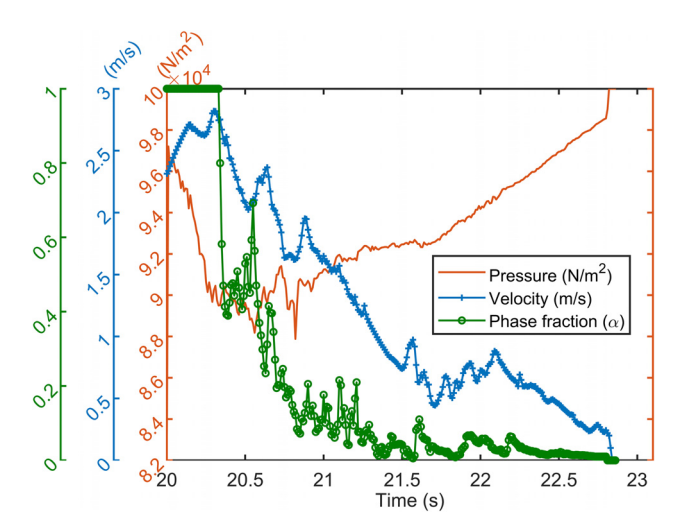


Fig. 15 Zoom-in of Fig. 14

Figure 7 shows the variation of velocity and pressure at section A-A (shown in Fig. 1) according to the water level in the storage tank under no-leakage conditions. With the decrease of water level from 2 m to 1 m, the water velocity decreases from 2.28 m/s to 1.65 m/s. The reduction in water velocity is due to a decrease in induced force [40]. This can also be visualized by the reduction in pressure from 83800 N/m² to 78650 N/m². The siphon flow continues until the water level reaches the pipe inlet elevation, i.e., at an elevation of 1 m in the storage tank.

Figure 8 shows the isobaric surface plots for atmospheric pressure under no-leakage conditions for various times (at $t = 6 \, \text{s}$, $t = 32 \, \text{s}$, $t = 60 \, \text{s}$, and $t = 92 \, \text{s}$). At $t = 6 \, \text{s}$, the level atmospheric pressure in the storage tank is at $2 \, \text{m}$, whereas it is at $1.45 \, \text{m}$ and $1.02 \, \text{m}$ in the upgoing and the downgoing limb of the siphon pipe, respectively. With the decrease in the water level in the tank, the shift of the isobaric surface shows the shift of positive and negative pressure regions in the system.

Comparison of CFD numerical, analytical, the energy equation, and the experimental results of water level and discharge time traces are shown in Fig. 9. The energy equation uses the Eq. (12) and Eq. (14) to determine H and Q time traces, with the updated value of friction factor (f) corresponding to the velocity of flow at that instance, whereas the analytical solution uses the same equations with a constant value for the friction factor (f). As observed

in Fig. 9, the time trace of water level and discharge rate obtained using the analytical, energy equation, and the numerical model agrees very well with the experimental data. The CFD simulations started with motionless water conditions, whereas in the experiments, the butterfly valve at the siphon outlet takes a considerable time (\sim 15 s) to fully open. This gradually increases flow in the experiments, whereas it rises suddenly in the CFD model.

Figure 10 compares the CFD results neglecting surface tension and considering surface tension ($\sigma = 0.072$ N/m). As observed, the results are identical. This is not surprising as capillary forces are insignificant compared to the viscous forces in the siphon system under the given configuration. The Capillary number (Ca) represents the relative effect of drag force with surface tension forces acting across an interface between the water and air phase. A flow dominated by capillary force usually has Ca $\leq 10^{-5}$ [41]. For the siphon system in this work, Ca ranges from 0.0197 to 0.0346.

The mesh convergence study results are shown in Fig. 11. Figure 11 shows that the coarse mesh produces unacceptable results, whereas the medium and fine meshes agree well with the experimental data. Therefore, considering the noticeable decrease in computational time from the fine mesh to the medium and the negligible differences in their performance, the medium mesh was used for the rest of the simulations. The medium mesh (mesh 2) had 2,048,751 cells with 1,907,711 hexahedra, 77,722 polyhedra, and 63,318 prisms. The overall mesh quality was acceptable, with a maximum skewness of 2.5 and an average nonorthogonality of 6.6 deg.

Siphon With Leakage Conditions. This section discusses the impact of pipe leakage on the siphon break phenomena using three holes at different positions, one at the top portion of the siphon pipe (case-1), the second at the upper side of the downgoing limb of the pipe (case-2), and third at the lower part of the downgoing limb of the pipe (case-3). All the siphon pipe leakage simulations are performed in two parts. For the first 20 s, no leakage is provided. This was done to develop the siphon flow for a specific time interval. Later, to mimic the accidental leakage, the generated data from the first simulation was used as an initial condition for the second part in which a leak was introduced with an extended cylindrical domain. An extended cylindrical computational domain was provided at the leak outlet to avoid imposing an atmospheric pressure at the leak outlet, which leads to artificial instabilities in the siphon. The extended domain is open to the atmosphere with a total pressure value set to 101,600 N/m².

Figure 12 shows the air—water phase fraction at the center plane for various times after 20 s for the leakage case-1. At (a) t = 20.1 s, the air entered the siphon pipe and started flowing with the water flow. From (b) t = 20.3 s to (f) t = 20.9 s, the ingested air was moving at the outlet of the pipe with siphoning water. At (g) t = 21.5 s, the middle portion of the siphon top and downgoing limb of the pipe is mostly filled with air, causing interruption of siphon flow. Finally, at (h) t = 22.4 s, the remaining water from the upgoing and downgoing limbs of the pipe falls back to the storage tank and toward the outlet, respectively.

Figure 13 shows the 3D free surface plots at several instances for the leakage case-1. This figure shows complex flow fields promoted by air penetration. From t = 20.1 s to t = 20.4 s (Figs. 13(a) - 13(c)), the penetrated air advances along with the siphoning water. As air advances toward the downgoing limb of the pipe, the velocity of the free water surface increases. At (d) t = 20.6 s, a swirling of free water surface generated by the ingressed air is observed. After that, high-velocity air entering through the hole causes a cavity on the free water surface and interrupts the siphoning.

Figure 14 shows the complete time trace of water velocity and the pressure at section A-A for leakage case-1. The leakage is specified at $t = 20 \, s$. For the first 20 s, a reduction in water velocity and pressure is observed. At $t = 20 \, s$, a sharp rise in the pressure from $82620 \, \text{N/m}^2$ to $97210 \, \text{N/m}^2$ is observed due to ingressed air. A similar increasing trend of water velocity was observed as it

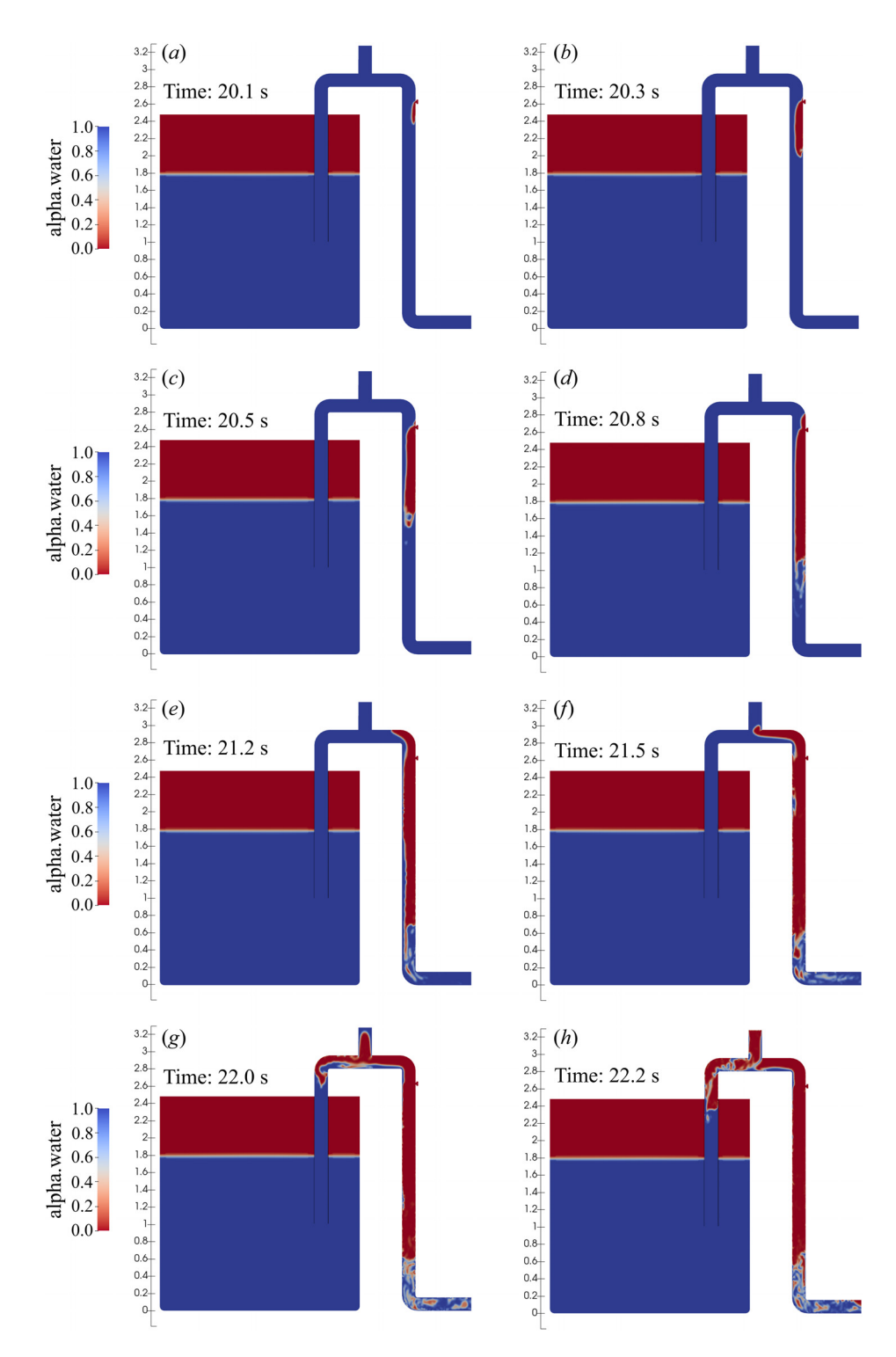


Fig. 16 Water volume fraction for leakage case-2 at eight different times: (a) $20.1 \,\mathrm{s}$, (b) $20.3 \,\mathrm{s}$, (c) $20.5 \,\mathrm{s}$, (d) $20.8 \,\mathrm{s}$, (e) $21.2 \,\mathrm{s}$, (f) $21.5 \,\mathrm{s}$, (g) $22.0 \,\mathrm{s}$, and (h) $22.2 \,\mathrm{s}$

increased from 2.3 m/s to 2.8 m/s. Figure 15 shows, at t = 21.71 s the velocity reaches 0.44 m/s. The water velocity undergoes reduction, and pressure increases with successive oscillations and finally reaches the end of the simulation, i.e., velocity goes to zero as pressure approaches atmospheric pressure. Successive oscillations in velocity and pressure are observed due to the remaining water from the extended sight tube falling back toward the outlet. This can be seen in Figs. 12(f)-12(h) and Figs. 13(i)-13(l).

Figure 16 shows the air—water phase fraction at the center plane for leakage case-2. At (a) t = 20.1 s to (d) t = 20.8 s, the advancement of air through a leak in the downgoing limb of the siphon

pipe can be seen. The advancement of penetrated air is smooth, which can also be visualized using a 3D air—water interface surface plot in Fig. 17. At (e) t=21.2 s, the downgoing pipe is mostly filled with ingressed air.

Figure 18 shows the complete time trace of water velocity and pressure at section A-A for leakage case-2. A completely different evolution of water velocity was observed for case-2 than for case-1. Figure 19 shows that although pressure increases after leakage (t = 20 s), the water velocity reduces gradually and reaches almost zero (0.043 m/s at t = 21.08 s). Then, after successive oscillations, it reaches zero. The pressure shows a

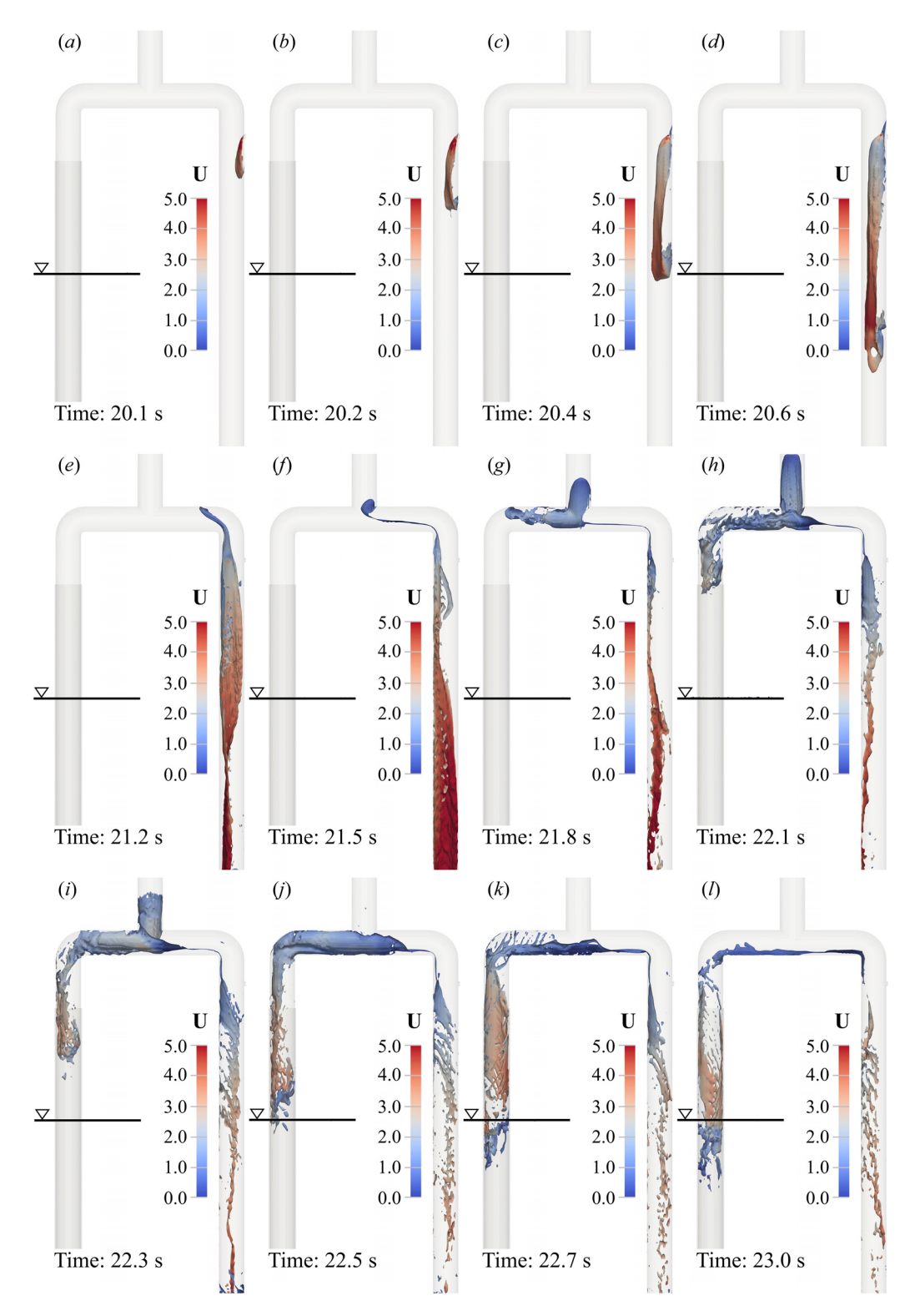


Fig. 17 Siphon leakage case-2. 3D air—water interface surface plots at twelve times: (a) $20.1 \, s$, (b) $20.2 \, s$, (c) $20.4 \, s$, (d) $20.6 \, s$, (e) $21.2 \, s$, (f) $21.5 \, s$, (g) $21.8 \, s$, (h) $22.1 \, s$, (i) $22.3 \, s$, (j) $22.5 \, s$, (k) $22.7 \, s$, and (l) $23.0 \, s$

similar trend as case-1, which shows a sudden increase from 82790 N/m² to 95920 N/m² and then undergoes a drop and finally reaches atmospheric pressure through successive oscillations. As observed, the oscillation in the pressure is smooth in case-2 compared to case-1, which causes a less induced force on the water, causing rapid breakage of the siphon flow. Similar to case-1, these oscillations in velocity and pressure are observed due to the remaining water from the extended sight tube falling back toward

the outlet. This can be seen in Figs. 16(f)-16(h) and Figs. 17(i)-17(l).

Figure 20 shows the results for case-3, in which leakage is present below the hydraulic grade line. The initial position of the hydraulic grade line in the downgoing limb of the pipe is at 1 m (Fig. 8). Figure 20(b) shows the location and size of the leak $(d_l = 1 \text{ inch})$, where d_l is the diameter of the leak hole. At t = 0 s to t = 44 s, the hydraulic grade line is above the leakage, causing

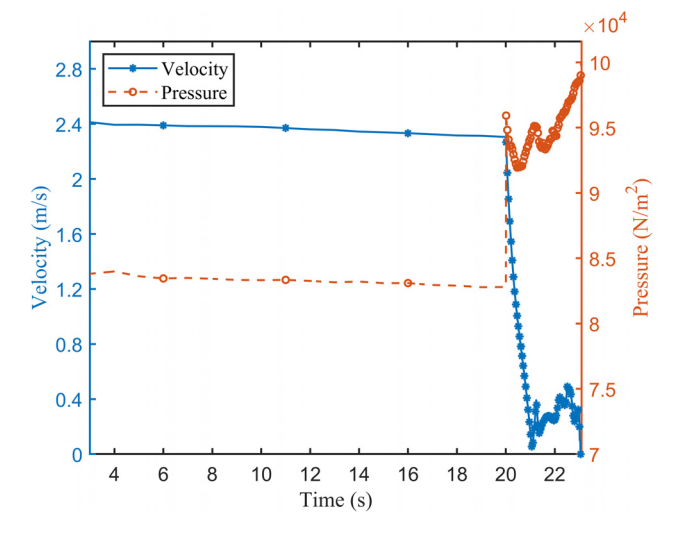


Fig. 18 Water velocity and pressure time trace at section A-A for leakage case-2

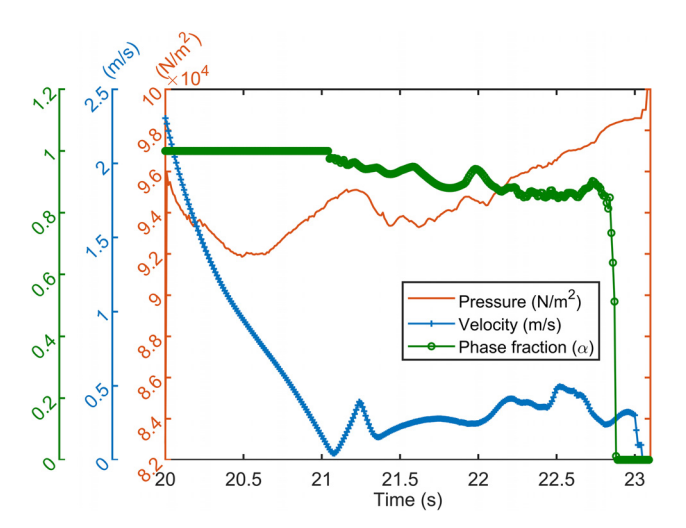


Fig. 19 Zoom-in of Fig. 18

water to flow from the leakage. Velocity vectors show the movement of water through leakage in Fig. 20(a). At t = 45 s, the hydraulic grade line reaches the leakage and starts building the suction pressure. This can be seen in Fig. 20(c), as the atmospheric air starts entering the pipe. As time advances, more air starts entering the pipe as the hydraulic grade line falls further below the leakage, causing an increase in suction pressure. Even though the air had entered the pipe, no siphon breakage was observed immediately, as the inertial force of water coming toward the outlet caused air to move along with it. Figure 20(d)shows the advancement of ingressed air by siphoning water toward the outlet. Figure 23 shows the complete time trace of water velocity and pressure at section A-A for leakage case-3. As shown in Fig. 23, for the first 45 s, a reduction in water velocity (2.45 m/s to 2.1 m/s) and pressure (83305.3 N/m² to 80868.5 N/m²) is observed, as no air is ingested into the siphon pipe (hydraulic grade line is above the leakage). At $t = 45 \,\mathrm{s}$, air starts entering through hole, and unlike in case-1 and case-2, completely different behavior was observed. From time t = 45 s to t = 55 s, even though the air was ingested into the system, no significant variations in velocity and pressure were observed, as the quantity of air ingested into the siphon pipe was significantly less, and this ingested air immediately gets carried away to the outlet with the siphoning water. As time advances, more air starts entering the pipe, causing velocity to reduce, whereas pressure increases slowly from t = 56 s to t = 75 s. As shown in Fig. 24, the ingested air reaches section A-A at t = 78.3 s. Once the ingested air reaches the upper limb, it takes much less time ($\approx 2.7 \, \text{s}$) to cause complete siphon breakage, similar to case-1 and case-2. The complete air-water phase fraction at the center plane and a 3D air-water interface surface plot for case-3 can be seen in Figs. 21 and 22, respectively. Unlike case-1 and case-2, the leakage position in case-3 is far away from the upper part of the inverted U shape of the pipe, allowing it further time to cause complete siphon breakage.

Conclusion

This paper studied detailed hydrodynamic characteristics of a siphon system numerically, analytically, and experimentally. Although siphon breakage can be predicted using the energy equation (knowing the location of leakage related to HGL), detailed insights into the hydrodynamic characteristics of siphon flow

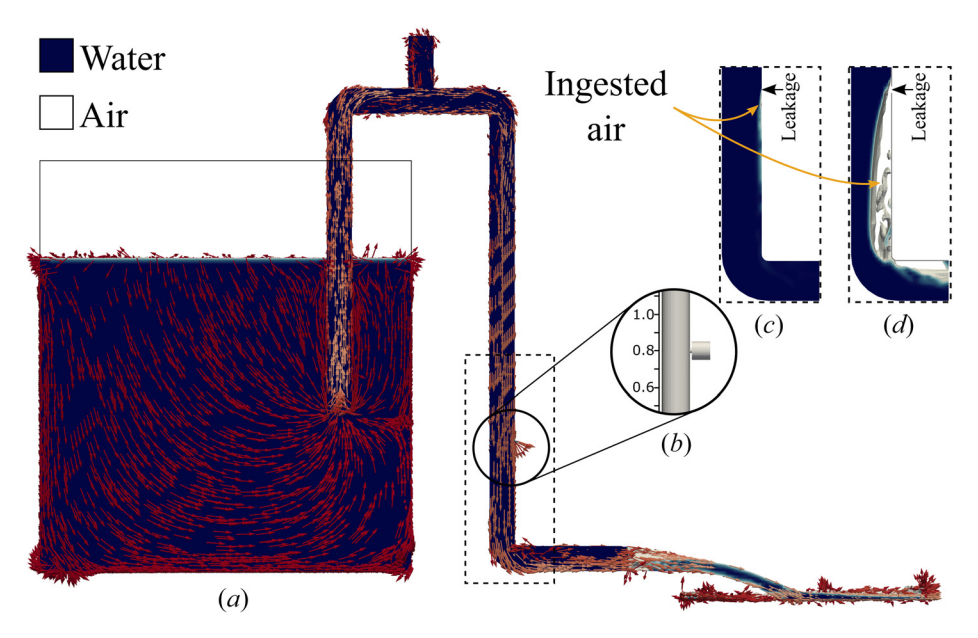


Fig. 20 Simulation results for the case-3 (leakage below hydraulic grade line): (a) instantaneous velocity vectors, (b) location of leakage, (c) air–water phase fraction at $t = 45.0 \, \text{s}$, and (d) air–water phase fraction at $t = 63.0 \, \text{s}$

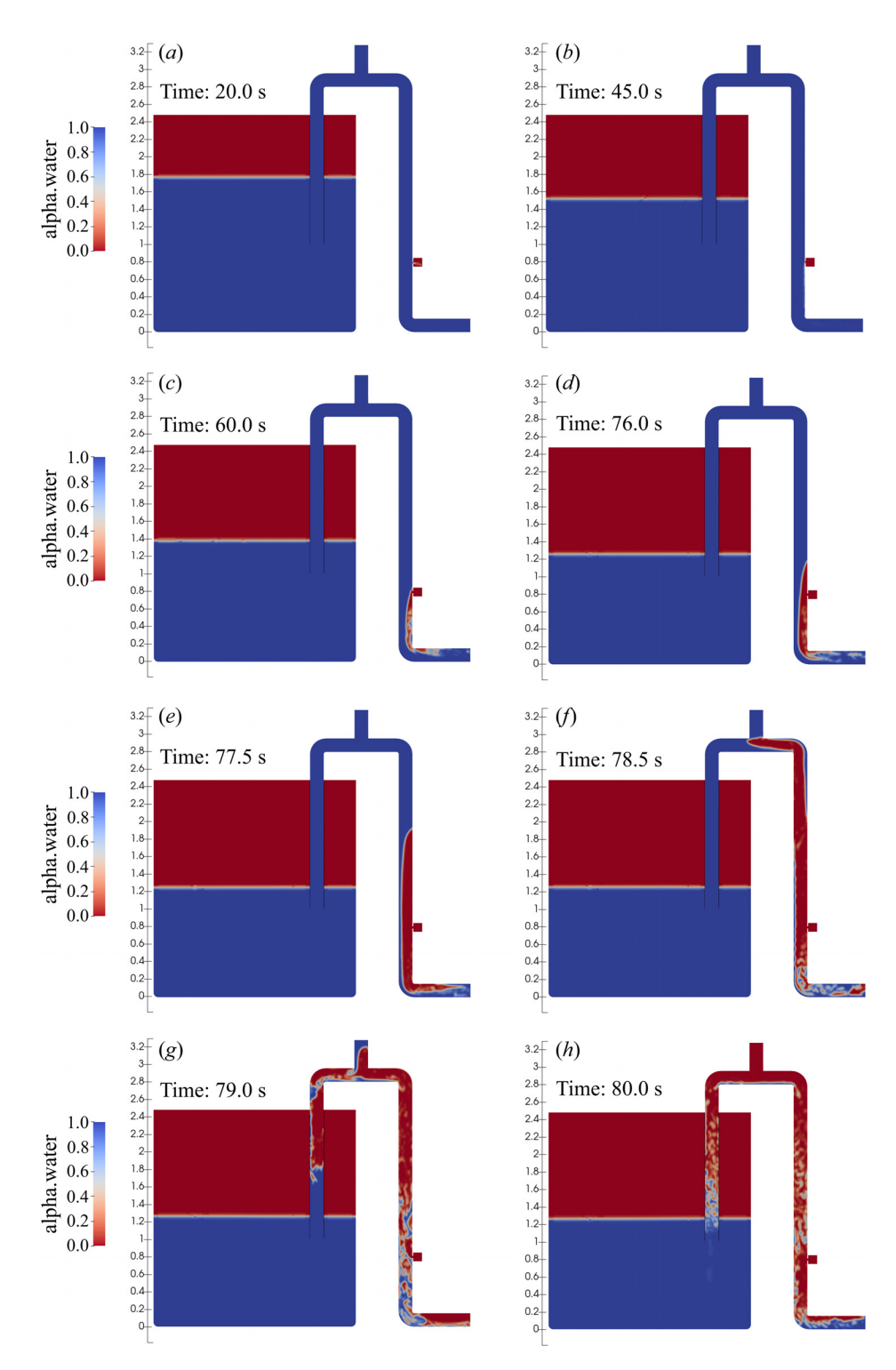


Fig. 21 Water volume fraction for leakage case-3 at eight different times: (a) $20.0 \, s$, (b) $45.0 \, s$, (c) $60.0 \, s$, (d) $76.0 \, s$, (e) $77.5 \, s$, (f) $78.5 \, s$, (g) $79.0 \, s$, and (h) $80.0 \, s$

under leakage can be investigated using a 3D numerical model. Detailed understanding of two-phase dynamics using 3D numerical simulations helps understand the role of the location of the leakage in maintaining siphon flow. A detailed 3D computational model for the no-leakage condition was developed to investigate the siphon break phenomenon associated with a leakage in the siphon pipe. Two leakages (leak hole diameter of 1 inch) at different locations were investigated; one at the horizontal section at the top of the inverted U pipe and another at the downgoing limb of the pipe. Both these locations are chosen above the hydraulic

grade line of the siphon. In addition to this, one more leakage case was tested at the location below the hydraulic grade line.

The results demonstrate that, in general, a good agreement between numerical, analytical, energy equation, and experimental results were obtained for the siphon under the no-leakage condition.

The effects of leakage position on siphon performance were investigated numerically and compared using water velocity, pressure, and phase fraction transient data. Results show that the position of leakage influenced the flow dynamics. For the leakage at

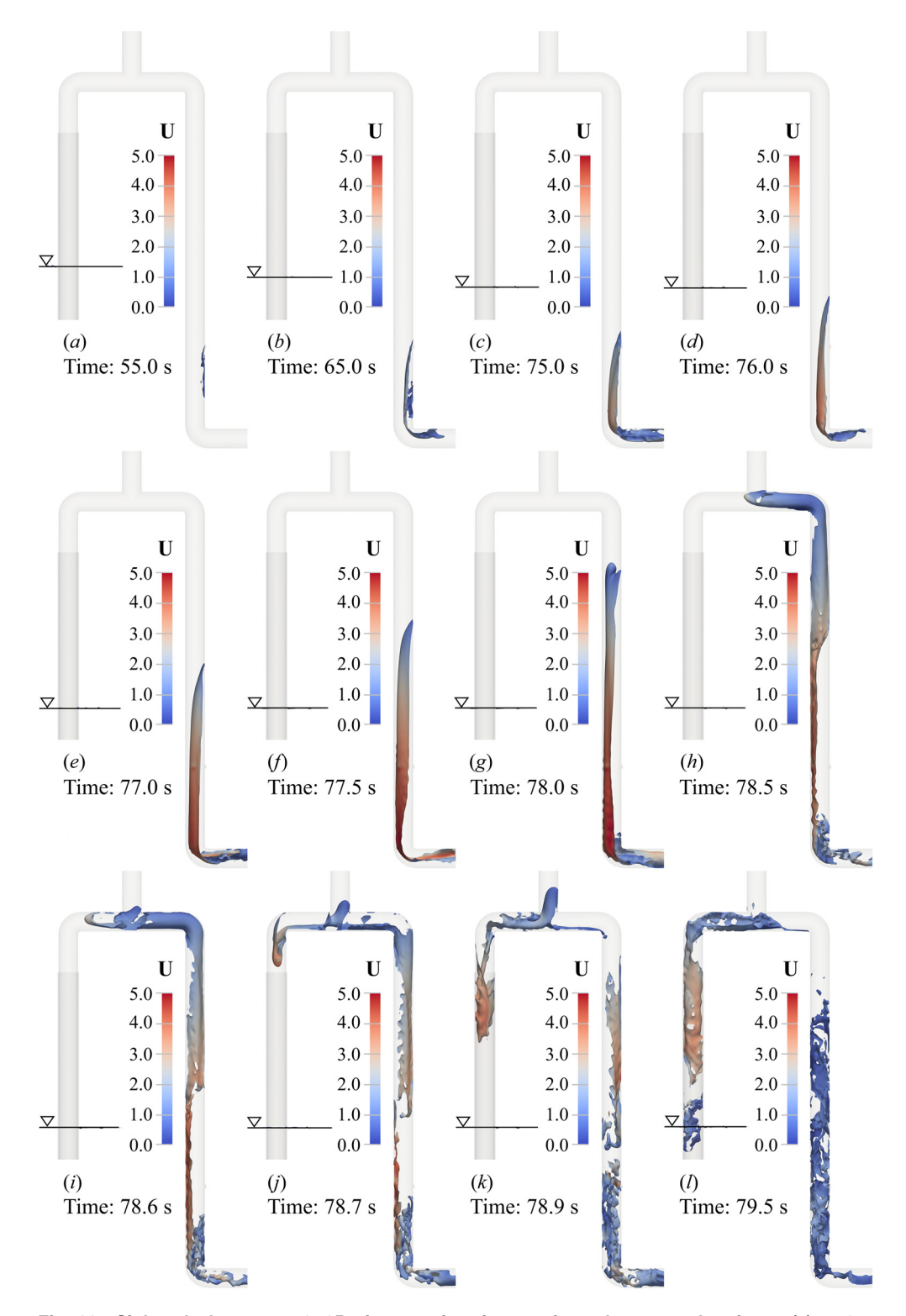


Fig. 22 Siphon leakage case-3. 3D air—water interface surface plots at twelve times: (a) $55.0 \, s$, (b) $65.0 \, s$, (c) $75.0 \, s$, (d) $76.0 \, s$, (e) $77.0 \, s$, (f) $77.5 \, s$, (g) $78.0 \, s$, (h) $78.5 \, s$, (i) $78.6 \, s$, (j) $78.7 \, s$, (k) $78.9 \, s$, and (l) $79.5 \, s$

the top horizontal portion of the siphon pipe (case-1), the water undergoes a sudden rise in the velocity immediately after the leakage, causing slightly more time to completely interrupt the siphon flow than in case-2 in which leakage is at the downgoing limb of the pipe. In leakage case-1 and case-2, the leakages are present above the hydraulic grade line, causing air to ingest into the pipe, leading to siphon breakage. The positions of leakages in case-1

and case-2 were close to the upper horizontal section of the siphon pipe, which makes them the favorable condition for siphon breakage as ingested air immediately reaches the inverted U shape of the pipe, causing flow interruption.

It is observed that, as long as leakage is below the hydraulic gradient line (the initial state in case-3), no air is allowed to enter the pipe due to the outgoing flow of water from the siphon. This

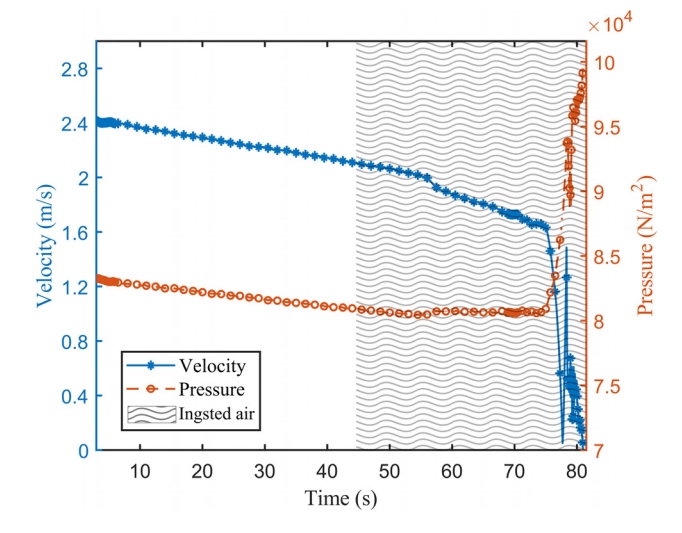


Fig. 23 Water velocity and pressure time trace at section A-A for leakage case-3

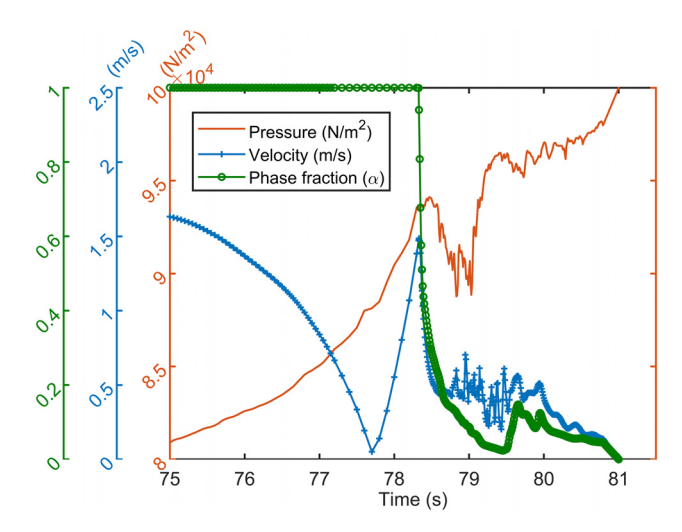


Fig. 24 Zoom-in of Fig. 23

leakage acts as another discharge point for the siphon flow. When the hydraulic grade line reaches the leakage, the air starts ingesting the pipe, similar to case-1 and case-2. However, unlike previous cases (case-1 and case-2), the leakage position in case-3 is far away from the upper horizontal section of the siphon pipe, causing the removal of ingested air with outgoing water flow without immediate siphon breakage. The pressure inside the pipe at the top horizontal section increases very slowly despite the air ingress. This is primarily due to the position and size of the leakage. For the siphon breakage, it is crucial for the ingested air to reach the upper part of the inverted U shape of the pipe to cause flow interruption. It takes significant time for the ingested air to interrupt the siphon flow if the leakage location is far away from the upper horizontal section of the siphon pipe. Once the air reaches the upper part of the siphon, it immediately causes the siphon breakage, same as in case-1 and case-2.

Acknowledgment

This work was supported by the National Science Foundation through NSF/ENG/CBET under award No. 1805417 and through NSF/DBI/BIO under award No. 1820778. In addition, the authors would like to thank reviewers for their thoughtful comments.

Funding Data

• National Science Foundation (Award Nos. 1805417 and 1820778; Funder ID: 10.13039/100000001).

Nomenclature

A =area of the base of the storage tank (m²)

 $A_d =$ cross-sectional area of the siphon pipe (m²)

 $B_o = \text{Bond number}$

C =Courant number

Ca =Capillary number

 d_l = leakage hole diameter (m)

D = siphon pipe diameter (m)

f = friction factor

g = acceleration due to gravity (ms⁻²)

H = water elevation in the tank (m)

 H_0 = initial water level in the tank (m)

 h_f = total head loss due to pipe friction (m)

 $h_l = \text{sum of local head losses (m)}$

k = head loss coefficient for the pipe fittings

L = total length of the siphon pipe (m)

 P_1, P_2 = pressure at points 1 and 2, respectively (Nm⁻²) p_d = modified pressure (Nm⁻²)

 $Q = \text{discharge rate } (\text{m}^3 \text{s}^{-1})$

Re = Reynolds number

 $T = \text{deviatoric stress tensor (Nm}^{-2})$

 $u_r = \text{liquid-gas relative velocity (ms}^{-1})$

v = pipe cross-sectional averaged flow velocity (ms⁻¹)

 v_1 , v_2 = cross-sectional averaged velocities at points 1 and 2,

respectively (ms⁻¹) x = position vector (m)

 Z_1, Z_2 = elevation at points 1 and 2, respectively (m)

Greek Symbols

 α = liquid phase fraction

 $\gamma = \text{specific weight (Nm}^{-3})$

 ϵ = absolute roughness of the pipe inside wall (m)

 $\kappa = \text{local curvature of the free surface}$

 $\mu = \text{dynamic viscosity (kgm}^{-1}\text{s}^{-1})$

 $\rho = \text{density (kgm}^{-3})$

 $\sigma = \text{surface tension (Nm}^{-1})$

 $\chi = constant parameter$

References

- [1] Qin, L., Leon, A. S., Bian, L., Dong, L.-L., Verma, V., and Yolcu, A., 2019, "A Remotely-Operated Siphon System for Water Release From Wetlands and Shallow Ponds," IEEE Access, 7, pp. 157680–157687.
 [2] Leon, A. S., and Verma, V., 2019, "Towards Smart and Green Flood Control:
- Remote and Optimal Operation of Control Structures in a Network of Storage Systems for Mitigating Floods," 2019 ASCE-EWRI World Environmental & Water Resource Congress, May 19–23, Pittsburgh, PA, pp. 177–189.
- [3] Ghosh, S. N., 2014, Flood Control and Drainage Engineering, 4th ed., CRC Press, Taylor & Francis Group, London.
 [4] Potter, A., and Barnes, F. H., 1971, "The Siphon," Phys. Educ., 6(5), pp.
- 362-366.
- [5] Hughes, S. W., 2010, "A Practical Example of a Siphon at Work," Phys. Educ., 45(2), pp. 162-166. [6] Ramette, J. J., and Ramette, R. W., 2011, "Siphonic Concepts Examined: A Carbon
- Dioxide Gas Siphon and Siphons in Vacuum," Phys. Educ., 46(4), pp. 412–416. [7] Richert, A., and Binder, P. M., 2011, "Siphons, Revisited," Phys. Teach., 49(2), pp. 78-80.
- [8] Ervine, D., 1976, "The Design and Modelling of Air-Regulated Siphon Spillways," Proc. Inst. Civ. Eng., 61(2), pp. 383-400.
- [9] Ervine, D. A., and Oliver, G. C. S., 1980, "The Full-Scale Behavior of Air-Regulated Siphon Spillways," Proc. Inst. Civ. Eng., 69(3), pp. 687-706.
- [10] Babaeyan-Koopaei, K., Valentine, E. M., and Ervine, D. A., 2002, "Case Study on Hydraulic Performance of Brent Reservoir Siphon Spillway," J. Hydraulic Eng., 128(6), pp. 562-567.

- [11] Viridi, S., Suprijadi, Khotimah, S. N., Novitrian., and Masterika, F., 2011, "Self-Siphon Simulation Using Molecular Dynamics arXiv:1104.1847.
- [12] Cai, Y.-l., Sun, H.-y., Shang, Y.-Q., and Xiong, X.-l., 2014, "An Investigation of Flow Characteristics in Slope Siphon Drains," J. Zhejiang Univ. Sci. A, **15**(1), pp. 22–30.
- [13] Leon, A. S., and Alnahit, A., 2016, "A Remotely Controlled Siphon System for Dynamic Water Storage Management," IAHR International Symposium on Hydraulic Structures, June 27-30, 2016, Portland, OR, pp. 177-189.
- [14] Aydin, M., Öztürk, M., and Yücel, A., 2015, "Experimental and Numerical Investigation of Self-Priming Siphon Side Weir on a Straight Open Channel," Flow Meas. Instrumentation, 45, pp. 140-150.
- [15] Kang, S. H., Ahn, H. S., Kim, J. M., Joo, H. M., Lee, K.-Y., Seo, K., Chi, D. Y., Yoon, J., Jeun, G. D., and Kim, M. H., 2013, "Experimental Study of Siphon Breaking Phenomenon in the Real-Scaled Research Reactor Pool," Nucl. Eng. Des., 255, pp. 28–37.
- [16] Park, I. K., Yoon, H. Y., and Park, H. B., 2018, "Numerical Approach to Siphon Break Phenomena in a Research Reactor Pool Using the Cupid Code," Nucl. Eng. Des., 326, pp. 133–142.
- [17] Ramajo, D. E., Corzo, S. F., and Nigro, N. M., 2020, "Numerical Simulation of Siphon Breaker Systems for Open-Type Research Reactors," ASME J. Nucl. Eng. Radiat. Sci., 6(2), p. 021202.
- [18] Direct, C., 2018, OpenFOAM 6.0.
- [19] Kamand, F. Z., 1988, "Hydraulic Friction Factors for Pipe Flow," J. Irrig. Drain. Eng., 114(2), pp. 311–323.
- [20] Bernuth, R. D. V., 1990, "Simple and Accurate Friction Loss Equation for Plastic Pipe," J. Irrig. Drain. Eng., 116(2), pp. 294–298.
- [21] Romeo, E., Royo, C., and Monzón, A., 2002, "Improved Explicit Equations for Estimation of the Friction Factor in Rough and Smooth Pipes," Chem. Eng. J., 86(3), pp. 369-374.
- [22] De Marchi, G., 1950, Idráulica: Basi Scientifiche E Applicazioni Tecniche, Ulrico Hoepli, Milano.
- [23] Christodoulou, G. C., 1991, "Drop Manholes in Supercritical Pipelines," J. Irrig, Drain, Eng., 117(1), pp. 37–47.
 [24] Neto, O. R., de Miranda, J. H., Frizzone, J. A., and Workman, S. R., 2009,
- "Local Head Loss of Non-Coaxial Emitters Inserted in Polyethylene Pipe,"
- Trans. ASABE, **52**(3), pp. 729–738.

 [25] Haaland, S. E., 1983, "Simple and Explicit Formulas for the Friction Factor in Turbulent Pipe Flow," ASME J. Fluids Eng., **105**(1), pp. 89–90.

- [26] Weller, H. G., Tabor, G., Jasak, H., and Fureby, C., 1998, "A Tensorial Approach to Computational Continuum Mechanics Using Object-Oriented Techniques," Comput. Phys., 12(6), pp. 620–631.
- [27] Erwee, M., Reynolds, Q., Zietsman, J., and Bezuidenhout, P., 2019, "Multiphase Flow Modelling of Lancing of Furnace Tap-Holes: Validation of Multiphase Flow Simulated in OpenFOAM®," J. Southern Afr. Inst. Min. Metall., 119(6), pp. 551–556. [28] Foundation, T. O., 2015, OpenFOAM v6 User Guide.
- [29] Hirt, C., and Nichols, B., 1981, "Volume of Fluid (Vof) Method for the Dynamics of Free Boundaries," J. Comput. Phys., 39(1), pp. 201-225.
- Berberović, E., van Hinsberg, N. P., Jakirlić, S., Roisman, I. V., and Tropea, C., 2009, "Drop Impact Onto a Liquid Layer of Finite Thickness: Dynamics of the Cavity Evolution," Phys. Rev. E, 79(3), p. 036306.
- [31] Berberović, E., Roisman, I. V., Jakirlić, S., and Tropea, C., "Computational Study of Hydrodynamics and Heat Transfer Associated With a Liquid Drop Impacting a Hot Surface," Computational Fluid Dynamics 2010, A. Kuzmin, ed., Springer, Berlin Heidelberg, pp. 543-548.
- [32] Scheufler, H., and Roenby, J., 2021, "Twophaseflow: An Openfoam Based Framework for Development of Two Phase Flow Solvers," arXiv:2103.00870.
- [33] Wilcox, D. C., 1993, Turbulence Modelling for CFD, DCW Industries, La Cañada.
- [34] Launder, B., and Spalding, D., 1974, "The Numerical Computation of Turbulent Flows," Comput. Methods Appl. Mech. Eng., 3(2), pp. 269-289.
- [35] Hager, W. H., 2012, "Wilfrid Noel Bond and the Bond Number," J. Hydraulic Res., 50(1), pp. 3-9.
- [36] Ding, M., and Kantzas, A., 2007, "Capillary Number Correlations for Gas-Liquid Systems," J. Can. Pet. Technol., 46(02), p. 02.
- [37] Yeoh, G., and Tu, J., 2010, Solution Methods for Multi-Phase Flows, Butter-
- worth-Heinemann, Oxford, 12, chap. 3, pp. 95–242. Van Leer, B., 1997, "Towards the Ultimate Conservative Difference Scheme," J. Comput. Phys., 135(2), pp. 229–248.
 [39] Verma, V., 2021, "Low Cost and Reliable Integrated Hardware and Software
- Framework for Remotely Operated Water Release From Storage Units," Ph.D.
- Dissertation, Florida International University, Miami. FL. [40] Seo, K., Kang, S. H., Kim, J. M., Lee, K.-Y., Jeong, N., Chi, D.-Y., Yoon, J., and Kim, M. H., 2012, "Experimental and Numerical Study for a Siphon Breaker Design of a Research Reactor," Ann. Nucl. Energy, **50**, pp. 94–102. [41] Günther, A., and Jensen, K. F., 2006, "Multiphase Microfluidics: From
- Flow Characteristics to Chemical and Materials Synthesis," Lab Chip, 6(12), pp. 1487-1503.